




## Seismic and Aseismic Preparatory Processes Before Large Stick–Slip Failure

GEORG DRESEN,<sup>1,4</sup>  GRZEGORZ KWIA TEK,<sup>1,5</sup> THOMAS GOEBEL,<sup>2</sup> and YEHUDA BEN-ZION<sup>3</sup>

**Abstract**—Natural earthquakes often have very few observable foreshocks which significantly complicates tracking potential preparatory processes. To better characterize expected preparatory processes before failures, we study stick-slip events in a series of triaxial compression tests on faulted Westerly granite samples. We focus on the influence of fault roughness on the duration and magnitude of recordable precursors before large stick–slip failure. Rupture preparation in the experiments is detectable over long time scales and involves acoustic emission (AE) and aseismic deformation events. Preparatory fault slip is found to be accelerating during the entire pre-failure loading period, and is accompanied by increasing AE rates punctuated by distinct activity spikes associated with large slip events. Damage evolution across the fault zones and surrounding wall rocks is manifested by precursory decrease of seismic *b*-values and spatial correlation dimensions. Peaks in spatial event correlation suggest that large slip initiation occurs by failure of multiple asperities. Shear strain estimated from AE data represents only a small fraction (< 1%) of total shear strain accumulated during the preparation phase, implying that most precursory deformation is aseismic. The relative contribution of aseismic deformation is amplified by larger fault roughness. Similarly, seismic coupling is larger for smooth saw-cut faults compared to rough faults. The laboratory observations point towards a long-lasting and continuous preparation process leading to failure and large seismic events. The strain partitioning between aseismic and observable seismic signatures depends on fault structure and instrument resolution.

**Keywords:** Earthquakes, rupture, stick–slip tests, seismic, aseismic.

### 1. Introduction

Recent seismic and geodetic studies of large earthquakes at plate-bounding faults suggest potential preparation phases extending for months before the main shocks occurred. The observations show pronounced interaction of seismic foreshocks and aseismic slip, low and decreasing seismic *b*-values in space–time and correlation of pre-seismic locking and coseismic slip distribution (Moreno et al. 2010, Schurr et al. 2014, Hasegawa and Yoshida 2015; Avouac 2015). Aseismic creep may occur episodically, punctuated by slow slip events and low frequency earthquakes (Socquet et al. 2017; Frank et al. 2018). Creep likely accommodates varying but significant portions of slip in plate-bounding faults during the seismic cycle (Pacheco et al. 1993; Scholz and Campos 2012). These observations suggest that deformation in fault zones leading to seismic ruptures consists of a long-lasting and largely aseismic preparation phase punctuated by seismic events. However, the earthquake preparation phase and its potential observables may vary significantly depending on tectonic and thermodynamic conditions and fault properties. This study has the aim to resolve some of the primary parameters that govern preparatory processes before fault slip in laboratory and nature.

A plethora of field studies analyze the generation and geologic evolution of faults (e.g., Scholz 2019). These studies show that progressive strain localization results in the formation of single or multiple slip zones embedded in less deformed damage zones. Natural faults including those associated with major plate-boundaries have finite width, roughness and segmentation (e.g., Ben-Zion and Sammis 2003). Complex failure sequences and stress transfer from earthquakes on other faults produce additional local

<sup>1</sup> Helmholtz Centre Potsdam, German Research Centre for Geosciences GFZ, Potsdam, Germany. E-mail: dre@gfz-potsdam.de; kwiatek@gfz-potsdam.de

<sup>2</sup> Department of Earth Sciences, Memphis Center for Earthquake Research and Information, University of Memphis, Memphis, USA. E-mail: thgoebel@memphis.edu

<sup>3</sup> Department of Earth Sciences, University of Southern California and Southern California Earthquake Center, Los Angeles, CA 90089-0740, USA. E-mail: benzion@usc.edu

<sup>4</sup> Institute of Earth and Environmental Sciences, Universität Potsdam, Potsdam, Germany.

<sup>5</sup> Department of Earth Sciences, Freie Universität Berlin, Berlin, Germany.

stress heterogeneities affecting the seismic source, energy release and rupture arrest (e.g., Ben-Zion et al. 2003, Ampuero et al. 2006, Rippberger et al. 2007). Major faults with > 100 km slip also have finite width, roughness, segmentation, and varying strengths that are expected to evolve with further deformation. Heterogeneous fault properties and evolving seismicity produce strong heterogeneities of the stress field persisting along the fault over the entire seismic cycle (e.g., Ben-Zion and Rice 1993; Mai and Beroza 2002; Ben-David and Fineberg 2011). The heterogeneities control seismic energy release during inter-seismic loading and rupture dynamics (e.g., Ampuero et al. 2006; Rippberger et al. 2007; Romanet et al. 2018) resulting, for example, in varying slip distributions and aftershock stress drops (Fletcher and McGarr 2006; Schmittbuhl et al. 2006; Delouis et al. 2002; Bouchon et al. 2013; Schurr et al. 2014; Hasegawa and Yoshida 2015; Abercrombie et al. 2017; Cocco et al. 2016). Field observations are largely in agreement with experimental and modelling studies, clearly demonstrating the strong influence of a complex fault structure and fault roughness on rupture processes (Candela et al. 2011; Goebel et al. 2012, 2017). In addition, dynamic effects during rupture propagation and arrest (e.g., Cochard and Madariaga 1994; Ben-Zion et al. 2012) may also lead to roughening of the stress field, and therefore influence the slip, slip rate, and stress drop distributions (e.g., Schmittbuhl et al. 2006).

Classical nucleation and rupture models focus on single seismic events on a large pre-existing fault. These models predict a stable sliding phase over a critical nucleation patch before dynamic rupture breaks away (Ida 1972; Dieterich 1978, 1979, 1992; Palmer and Rice 1973; Ohnaka 1992). A nucleation phase involving slow stable sliding leading to dynamic rupture in a two-stage process has been observed experimentally in stick–slip tests performed on blocks of PMMA, steel, glass, and rocks (e.g., Ohnaka and Shen 1999; Popov et al. 2010; Kammer et al. 2015). The nucleation phase may involve only slow aseismic slip or produce a series of foreshocks as is frequently observed in laboratory tests (Scholz et al. 1972, McLaskey and Kilgore 2013; McLaskey and Lockner 2014, Selvadurai and Glaser 2017; Passelegue et al. 2017). Foreshock activity before

large events has been widely reported (Reasenberg 1999; Bouchon et al. 2013, Brodsky and Lay 2014, Mignan 2014, Ellsworth and Bulut 2018, Trugman and Ross 2019). However, the occurrence of foreshocks has clear spatial dependency on temperature and other conditions (e.g., Zaliapin and Ben-Zion 2013, 2016; McGuire et al. 2005; Martínez-Garzón et al. 2019), and there are well-documented cases of moderate to large events such as the 2004 M6 Parkfield earthquake in CA or the 1999 M7.1 Duzce earthquake in Turkey with no detectable foreshock activity (Bakun et al. 2005; Roeloffs 2006; Wu et al. 2014).

Conceptual nucleation models capturing distinct foreshocks or weak precursor phases observed for some earthquakes have motivated cascade and pre-slip models (Ellsworth and Beroza 1995), implying a stable preparation phase of an upcoming mainshock, characterized by slow aseismic pre-slip or, alternatively, a growing cascade of interacting foreshocks. However, it seems difficult to isolate the nucleation phase of a larger event from the preceding and potentially long-lasting preparation phase (Durand et al. 2020).

Here we exploit the similarities between stick–slip laboratory tests (Brace and Byerlee 1966, McLaskey and Lockner 2014, Kwiatek et al. 2014b; Goebel et al. 2017) and natural earthquakes to analyze premonitory deformation processes leading to failure. We present results from a series of new laboratory tests focusing on the preparation of stick–slip events involving progressive shear localization and unlocking of faults with different roughness. We present compiled results on the evolution of statistical and seismic source characteristics in space and time such as AE hypocenter distributions, focal mechanism orientation variability, magnitude-frequency distributions, fractal and clustering properties. The results emphasize the complex interplay of localized aseismic deformation, episodic slow slip events and small-scale dynamic ruptures manifested as AEs. To demonstrate the role of fault structure in governing rupture preparation and partitioning between seismic and aseismic deformation, we compare experiments on fresh fracture surfaces resulting in rough faults, with pre-cut surfaces resulting in smooth planar faults.

## 2. Materials and Methods

### 2.1. Sample Material and Experimental Set-Up

We performed a series of stick–slip experiments on 4 samples cored from the same block of Westerly granite. This rock type consists of 28% quartz, 33% plagioclase, 33% K-feldspar, 5% mica with an average grain size of 750  $\mu\text{m}$  (Goebel et al. 2012). Initial porosity was < 2%. Cylindrical samples were precision ground to 102–107 mm in length and a diameter of 40–50 mm. Samples were dried in an oven for several days before placing them in a rubber jacket to insulate them from the oil confining medium in the pressure vessel. For deformation tests, confined samples were placed in a servo-controlled Material Testing System (MTS) 4600 kN loading frame. A summary of experimental data is shown in Table 1.

To produce rough faults, intact specimens were prepared with 2.5 cm deep notches inclined at 30° to the specimen axis (Wgn05, Wgn19). Samples were then loaded axially at a confining pressure  $P_c$  of 75 MPa until shear failure occurred. Subsequently, confining pressure was raised to lock the faults and progressive axial loading at constant displacement rate of 0.33  $\mu\text{m/s}$  was used to induce stick slip events (Goebel et al. 2012). Faults with smooth sliding surfaces, were fabricated by cutting cylindrical samples at 30° inclination to the loading axis producing diagonal sawcuts (Wgc10, Wgc12). Stick–slip failure on rough and smooth faults was produced at confining pressures between 130–150 MPa.

Axial force was measured using an internal load cell with accuracy of  $\pm 0.05$  MPa. Piston displacement and axial shortening across the entire specimen was measured using a linear variable displacement transducer (LVDT) with sampling rate of 5 Hz. Local strains were measured using strain gages in axial and

circumferential direction as well as parallel and perpendicular to the faults in some tests forming a full bridge using MTS data acquisition system. Strain gages were glued directly to the sample surface at about 10 mm distance above and below the diagonal fault. Axial strain gage measurements were compared to the LVDT measurements and accuracy of strain gage measurements is estimated to be within  $\pm 0.5\%$ .

Up to 14 piezoelectric crystal P-wave transducers were placed in brass housings and glued directly to the sample surface using a low viscosity epoxy and appropriate holes in the rubber jacket. Piezoceramic PZT crystals were 5 mm in diameter with a thickness of 2 mm. The resonant frequency of the P-wave sensors was 1 MHz. The epoxy also served as a seal between sensor casing and rubber jacket (Fig. 1). Two additional P-wave transducers were placed in the top and bottom steel plugs. Full waveforms recorded continuously at the transducers were stored in a 16-channel transient recording system (DAXBox, PRÖKEL, Germany), with 16-bit digital amplitude resolution and 10 MHz sampling rate. Signals were amplified by 40 dB preamps (Physical Acoustic Corporation) and high-pass filtered at 100 kHz. Specific horizontal and vertical sensor pairs were used to derive time-dependent quasi-anisotropic and time-dependent P-wave velocity model composed of 5 horizontal and 1 vertical layers (e.g., Kwiatek et al. 2014a; b).

### 2.2. Data Analysis

#### 2.2.1 AE Locations, Magnitudes and Source Mechanisms

Ultrasonic pulses and AE signals were separated automatically during post-processing. To locate AE

Table 1

*Experimental data of specimens with rough (Wgn05, Wgn19) and smooth faults (Wgc10, Wgc12)*

Sample	$P_c$ (MPa)	Loading rate ( $\mu\text{m/s}$ )	No. AEs	No. AE per second	Average stress drop of slip events (MPa)	Average slip of events (mm) along the fault	Roughness (rms)
Wgn05	150	0.333	87,108	6.100	132	0.24	0.494
Wgn19	150	0.333	27,237	1.800	103	0.26	n/a
Wgc10	120	0.333	2259	0.1	146	0.34	0.014
Wgc12	133	0.333	1268	0.100	118	0.25	0.034

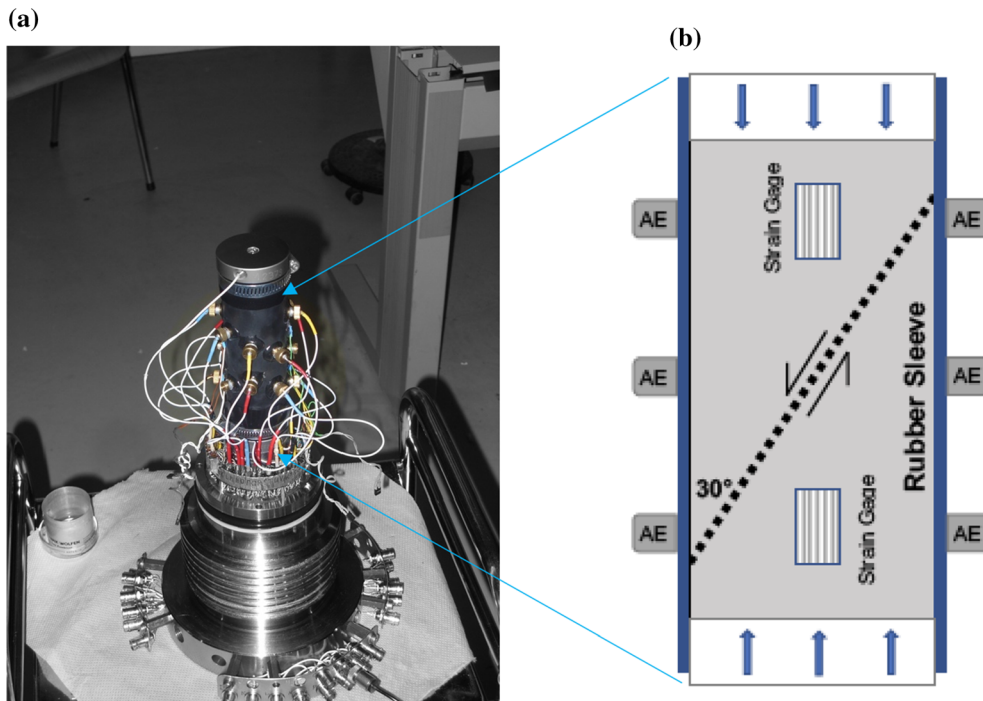


Figure 1

**a** Specimen assembly. The sample is contained in a rubber sleeve fixed to top and bottom end caps. The sleeve is perforated to allow placement of 14 piezoceramic transducers contained in brass housings. The transducers are glued directly to the specimen surface, sealed in the jacket with epoxy and signals are transmitted through cabled seals in the bottom plug. **b** Schematic cross section of sample assembly inside rubber jacket. Dotted line represents rough or sawcut fault

hypocenters, P-wave onset times were picked automatically using different criteria including Akaike's Information Criterion. AE hypocenter locations were estimated by minimizing travel time residuals using a hybrid grid search-downhill simplex algorithm using the time-dependent anisotropic velocity model. The estimated location accuracy of AE hypocenter is about  $\pm 2$  mm (e.g., Stanchits et al. 2006; Goebel et al. 2014).

After hypocenter determination, the relative AE magnitude was estimated as:

$$M_{AE} = \log_{10} \sqrt{\frac{1}{n} \sum_{i=1}^n (A_i R_i)^2}, \quad (1)$$

where  $A_i$  and  $R_i$  are the maximum amplitude and source-receiver distance for sensor  $i$ , respectively (e.g., Zang et al. 1998).

To compare cumulative seismic strain from AEs with shear strain during loading, we assumed seismic moment of the largest observed AE event, associated

with a large slip event along a rough fault, to be  $M_0 = 7$  Nm. This corresponds to a cm-scale source radius, in agreement with the maximum size of sheared asperities representing a fraction of the known lab-fault dimensions. The moment magnitudes of all remaining events were then calculated relative to the largest event. The moment magnitudes ( $M_W$ ) of AE events ranged from  $-8.5$  to  $-5.5$  comparable to those obtained in similar laboratory studies (McLaskey and Glaser 2012; Yoshimitsu et al. 2014).

The AE moment magnitudes were used to calculate seismic moment of AE events using a standard relation (Hanks and Kanamori 1979). Full moment tensor (FMT) inversion was performed using hybridMT software, based on first-motion P-wave amplitudes (Kwiatek et al. 2016). Before the FMT inversion, AE sensors were cross-calibrated using ultrasonic transmission measurements to remove effects of the coupling of AE sensors on recorded P-wave amplitudes and identify the correction for

incidence angle (see Kwiatek et al. 2014a, b, 2016 for details). The calculated FMTs were rotated into the principal coordinate system to obtain P(ressure), T(ension) and N(ull) axes directions, which in turn were used to calculate the orientation of nodal planes (strike/dip/rake). For a selected ensemble of AE events, we calculated the average 3D rotation angle between all unique pairs of AE focal mechanisms using their cardinal P and T axes. (e.g., Kagan 2007). The defined average rotation angles characterize the heterogeneity of focal mechanisms forming the ensemble (cf. Goebel et al. 2017).

### 2.2.2 Pair correlation function and fractal dimension

The spatial distribution of AE hypocenters in our experiments varies substantially as a function of roughness. To quantify this variability, we compute the Pair-Correlation-Function,  $C(r)$ , at all scales and for all AE event pairs,  $N$ , with separation distance,  $s$ , less than  $r$  (Kagan and Knopoff 1980; Grassberger 1983):

$$C(r) = N(s < r) / N_{\text{tot}}^2, \quad (2)$$

where  $N_{\text{tot}}$  is the total number of AE events within each experiment. Here we use only AE events in narrow time windows which are most representative of a given fault stress state. Through the selection of relatively narrow time windows, we can avoid events that repeatedly rupture the same fault patch which may be problematic for reliable estimates of fractal dimensions (Main 1992). After log-transformation, the Pair-Correlation-Function in Eq. (2) is approximately linear between 1 to 10 mm for our datasets, indicating that the spatial distributions of AEs are fractal within this distance-range (Henderson and Main 1992; Main et al. 1992; Main 1992; Wyss et al. 2004). The corresponding correlation dimension,  $D$ , was determined from the linear portion of logarithmically-binned Pair-Correlation-Functions, using a maximum-likelihood estimate and assuming Poissonian uncertainties in  $C$ :

$$C(r) = \beta r^D, \quad (3)$$

where  $\beta$  is a constant that depends on the overall number of events.

The distance,  $r$ , in Eq. (3) is bounded by a minimum ( $r_{\text{min}}$ ) and a maximum cut-off ( $r_{\text{max}}$ ) due to finite event density and finite sample size. The former is simply a function of the overall point-density relative to the size of the considered area, i.e.,  $r_{\text{min}} \sim 2 * \text{height} * \text{diameter} * (1/N)^{1/D}$ , where  $N$  is the total number of events and  $D$  is the dimension of the embedding Euclidean space (Kagan 2007). In practice, this minimum distance approximately coincides with  $r$  at  $C(r) \sim 2/N_{\text{tot}}^2$ , that is the distance at which the function is comprised of more than a single event. More details about the applied methods and robustness tests including the influence of overall event number and location uncertainty can be found in Goebel et al. (2017).

### 2.2.3 Magnitude Distributions and $b$ -Values

The AE magnitude distribution in our experiments can commonly be described by an exponential distribution with an exponent  $b$ . This  $b$ -value was determined by using a maximum-likelihood approach (Aki 1965).

$$b = 1/(\bar{M} - M_c) * \log(e), \quad (4)$$

where  $M_c$  is the magnitude of completeness, corrected for bin-size (Utsu et al. 1965, Guo and Ogata 1997) and  $\bar{M}$  is the mean magnitude above catalog completeness. For reliable  $b$ -value estimates, we require distributions to contain at least 150 AE events. Moreover, Eq. (4) shows that  $b$ -value estimates are sensitive to the estimated magnitude of completeness,  $M_c$ . To avoid biases, we use an objective approach to invert for both  $M_c$  and  $b$  through minimizing the misfit between observed and modeled distributions (Clauset et al. 2009; Goebel et al. 2017).

### 2.2.4 Seismic Coupling and Localization

In an effort to estimate shear strain on smooth and rough faults accommodated by seismic events, we follow Kostrov (1974; Eqs. (3, 10)). The mean shear deformation from  $N$  seismic events distributed in a damage zone volume  $\Delta V$  (i.e., Kostrov strain) is estimated as:



$$\Delta\varepsilon_{ij} = \frac{1}{2\mu\Delta V} \sum_{x=1}^N M_{ij}^x, \quad (5)$$

where  $\mu$  is the shear modulus of Westerly granite assumed to be 30 GPa. The volume of the damage zone,  $\Delta V$ , was determined by multiplying the elliptical surface area of the laboratory fault by the thickness of the damage zone,  $w_F$ . The former can directly be calculated based on the known sample dimensions and an angle of  $30^\circ$  between loading axis and fault surface. The damage zone thickness was derived from the 5th and 95th percentiles of across-fault AE event profiles with  $w_F \sim 4$  mm and  $\sim 10$  mm for saw-cut and rough faults, respectively. We assume that shear strain estimated from (5) corresponds to the cumulative shear strain from AE events,  $\gamma_{AE}$ , hosted in the fault and damage zone.

The total fault zone shear strain  $\gamma_F$  was estimated from the difference between the axial strain  $\gamma_{tot}$  and the local axial strain  $\gamma_{loc}$  of the sample. The axial strain  $\gamma_{tot}$  is an extrapolated linear elastic shortening of the sample and  $\gamma_{loc}$  is the local axial strain of the sample measured by the strain gages. The strain difference  $\gamma_{tot} - \gamma_{loc}$  was converted to fault parallel slip  $d_F$  and shear strain  $\gamma_F = d_F/w_F$ .

We then estimated the seismic coupling (Scholz and Campos 2012, McLaskey and Lockner 2014) during preparatory slip:

$$\chi = \gamma_{AE}/\gamma_F, \quad (6)$$

i.e., the ratio of shear strain from AE events,  $\gamma_{AE}$  to total shear strain in the fault zone  $\gamma_F$ .

### 3. Results

The data recorded during a series of triaxial compression tests on 4 samples with rough faults and smooth saw-cut faults include a series of up to 6 large, system-size stick-slip events (LSE) separated by loading cycles (Fig. 2). Between the LSE events, AE activity first drops following an Omori-Law type decay (Goebel et al. 2012) before loading of the sample assembly commences again about 20 s after the LSE stress drop. Here we analyze a selected number of these slip events from the tested samples focusing on processes controlling rupture preparation.

#### 3.1. Loading Curves of Sawcut and Rough Faults

The loading curves have distinctly different shapes for rough and smooth faults (Fig. 2). In general, rough faults show mostly non-linear stress strain curves with initial elastic loading up to a yield point for each cycle. Between yield points at about 85–90% peak stress,  $\sigma_p$ , and onset of the system-size slip event at  $\sigma_p$ , non-linear strain hardening is frequently interrupted by small, macroscopically visible slip events (Fig. 2). After several stick-slip cycles, fewer events with small stress drop are observed, suggesting that fault roughness decreased. Peak stress of subsequent stick-slip remains about constant; however, stress drops tend to increase with progressive slip events. In contrast, smooth faults show an extended period of almost linear elastic loading with minor strain hardening before abrupt onset of stick-slip failure resulting in LSEs. Deformation along smooth faults did not produce any small stress drop events as observed for rough faults. A macroscopic yield point before stress drop is more difficult to define from the loading curves prior to large slip events and typically is at  $> 90\%$   $\sigma_p$ . For sawcut samples, peak stresses increase markedly with successive stick-slip cycles and are up to 25% higher compared to rough faults. Similarly, stress drops of large slip events on smooth faults are significantly larger than on rough faults.

Large stress drops of system-size events on rough faults range from 100 to 150 MPa with average slip displacements of up to 0.26 mm (Table 1). Stress drops on smooth faults are up to 300 MPa and almost twice as large compared to rough faults. The corresponding slip displacements during individual events are as large as 0.5 mm. The MTS machine stiffness  $k_S$  is 360 MPa/mm but the combined loading stiffness is lower for both smooth and rough faults ( $k_L = 250$ – $300$  MPa/mm). Macroscopic stress drop events typically occur with slip rates ranging between 0.02 m/s to 20  $\mu$ m/s (Goebel et al. 2012).

#### 3.2. AE Activity, Hypocenter Locations and Focal Mechanisms

During loading between subsequent LSEs along rough faults, we observe an increase in AE activity

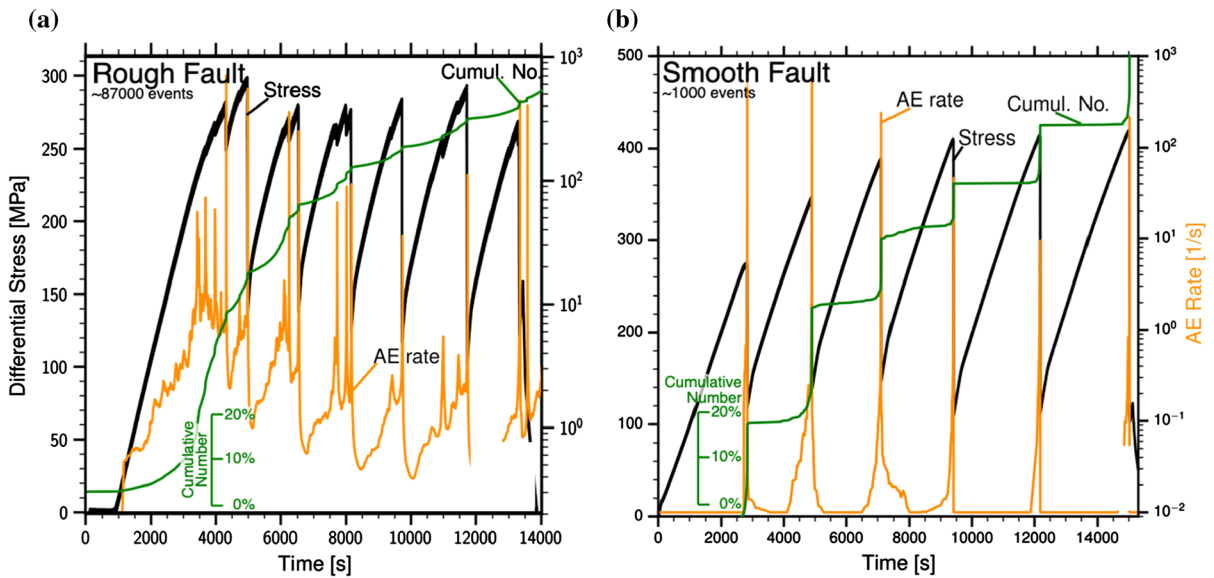


Figure 2

Differential stress-time plots for (a) rough fault produced by sample fracture of Wgn05 and (b) smooth saw-cut sample Wgc12. Differential stress is highlighted in black, AE rate in orange and normalized cumulative AE number in green

and the cumulative number of AEs approaching peak load (Fig. 2). The cumulative number of AEs during loading to LSE is up to 70 times larger for rough faults compared to sawcuts, also exceeding the number of events emitted during a single slip event. Before the onset of an LSE, the cumulative AE number increases in all samples but much more abruptly for smooth faults. With progressive slip events along rough faults, the increase in AE rate and cumulative AE number during leading to failure become less pronounced.

Increasing AE rates on rough faults are punctuated by intermittent bursts of AE activity prior to and during slip events. This suggests that AE rate and slip rate are correlated. The bursts in AE activity are superimposed on the background AE activity during inter-seismic loading that is increasing towards failure (Fig. 2). Large bursts in activity are linked to macroscopic slip events visible in the loading curve but with no clear relation to magnitudes of the stress drops (Fig. 2). This indicates that small episodic slip events preceding system-size failure produce enhanced AE activity. In contrast, numerous small AE bursts occurring during inter-seismic loading without noticeable macroscopic stress drops are

linked to small slip events contained in the fault surface. These events are too small to be resolved by displacement transducer, strain gages and external load cell. For sawcut samples, no discernable activity bursts comparable to those on rough faults are visible, except those related to large slip events, suggesting that during loading smooth faults are essentially locked for most of the inter-slip periods. Noticeable AE activity starts only very close to peak stress, when deviations of the stress-time curves from linear elastic behavior coincide with a rapid increase in both AE activity and cumulative number of AEs (Fig. 2), indicating onset of sliding along the fault.

AE hypocenter locations show non-stationary clusters activated along the fault trace for almost the entire loading cycle (Fig. 3). The spatial distribution of AE hypocenters clearly depends on fault roughness (Goebel et al. 2017). AE activity across the fault forms clusters changing in space and time with progressive loading, reflecting the change in contact area across the fault core. AE hypocenters prior to large slip events are more broadly distributed across the entire fault for smooth faults, suggesting more spatially-homogeneous stress compared to rough

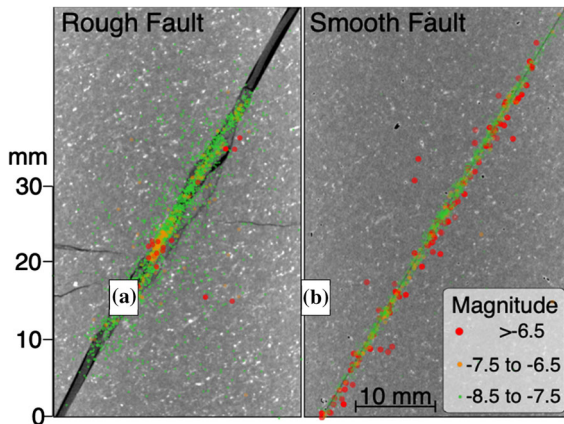


Figure 3

Computer-tomographic image of (a) rough fault and (b) sawcut. Symbols indicate AE hypocenter distribution along faults from a single slip episode; the estimated location error is  $\pm 2$  mm. Symbols are color-coded according to AE magnitudes. Note that damage zone in a rough fault is significantly wider compared to sawcut and fault structure is more complex

faults that show clustering of intermediate-size events reflecting localized asperities (Fig. 3).

The cores of fault zones in the experiments are surrounded by process or damage zones that form during initial fault propagation (Zang et al. 2000) and are reworked during multiple slip episodes. This is manifested by progressive clustering of events along the primary fault surface and a peak in event density distribution centered around the fault core. For smooth faults we find a narrow damage zone of

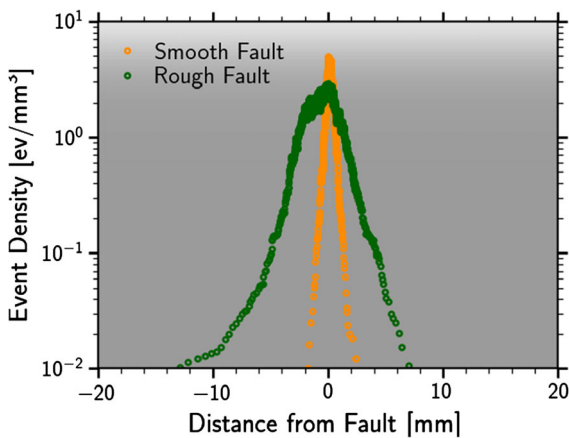


Figure 4

AE event density from experiments Wgn05 and Wgc12 projected in a fault-normal section. Rough faults show a wider damage zone compared to sawcut faults

about 2–3 mm width, which is of the order of the location accuracy for AE hypocenters (Fig. 4). In contrast, the AE event density distribution across rough faults indicates fault core widths of  $> 5$ –10 mm, with a power-law decay of event density towards the adjacent wall-rock (Fig. 4; Goebel et al. 2014). The width of the damage zone of rough faults in sections normal to the fault trace is 2–3 times that of sawcut faults (Kwiatek et al. 2014b).

However, the distribution of AE events surrounding the fault core is not stationary during a stick–slip cycle. We observe a distinct shift of hypocenter locations towards the fault core as peak stress is approached, expressed in a narrowing width of the fault-normal AE distribution (Fig. 5). During large slip events, the entire fault zone is activated resulting in a broad AE distribution. Once inter-slip loading of the fault restarts, the AE activity shifts from the outer damage zone towards the fault core with increasing stress highlighting progressive shear localization along rough faults prior to the next large slip event (Fig. 5).

We also find that orientations of AE focal mechanisms show significantly less variability for smooth faults compared to rough ones (Fig. 6a). Moreover, the progressive spatial localization of seismic activity towards the fault core when approaching failure is characterized by a reduced variability of fault plane orientations, both for sawcuts and rough faults (Fig. 6a). This decrease in

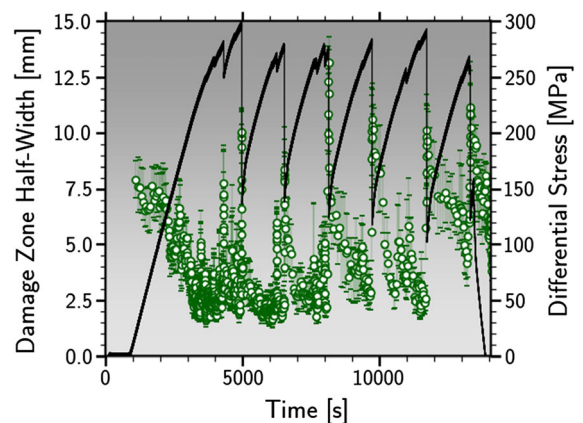


Figure 5

Damage zone half width centered at the fault trace (Wgn05) and estimated for a sliding time window during loading. During inter-slip loading, a shift of AE distributions towards the fault core reveals progressive localization of damage approaching failure



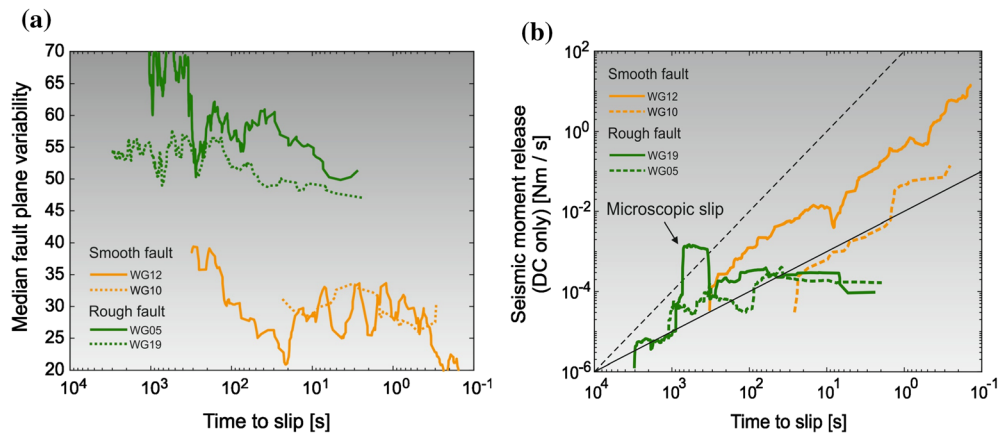


Figure 6

(a) Median fault plane variability of AE-derived focal mechanisms shows increasing similarity of focal mechanism towards failure, regardless of fault roughness. (b) Evolution of AE-derived seismic moment release rates leading-up to failure. The initial slope for all fault types is close to two (black dashed line) but significant differences between rough and smooth faults are observed closer to failure. For rough faults the seismic moment levels off and for smooth faults the exponent decreases to about 1 (black solid line)

variability of focal mechanisms with progressive loading is accompanied by a relative increase in double-couple components of FMTs (Kwiatek et al. 2014b), which is more clearly visible in the sawcut sample.

The double-couple components of moment release rates show a rapid temporal increase, which may be described by a power-law with an exponent of  $\sim 2$ . Since the axial displacement is linearly correlated with time, our observations indicate that the observed initial increase in moment rates scales with displacement squared. Prior to stick–slip failure, sawcut and rough faults show different trends. For smooth faults the slope decreases. This effect is visibly pronounced for rough faults for which moment rates level off prior to failure (Fig. 6b), suggesting that strain is partitioned progressively into aseismic deformation.

### 3.3. Changes in AE Magnitude-Frequency Distributions and Dimensional Parameters $D$ and $C$

As has been observed in many previous studies, AE magnitude-frequency distributions show a pronounced change approaching failure in stick slip tests. (Fig. 7a; Goebel et al. 2012, 2013, 2017). Decreasing  $b$ -values have been attributed to

increasing local stresses, crack growth and crack coalescence. Here we emphasize that the observed changes are a manifestation of progressive shear localization and are very similar to what has been observed previously in the formation of shear fractures in intact rocks (Stanchits and Dresen 2003).

In general,  $b$ -values decrease towards failure for both rough and sawcut faults, albeit with different trends. Changes in  $b$ -value during stick–slip cycles on rough faults involves two different time scales (Fig. 7a, b) (Goebel et al. 2013). The long-term trend of decreasing  $b$ -values during stress increase is interrupted by shorter episodes of accelerated  $b$ -value decrease with subsequent recovery. These episodes occur during inter-seismic loading and seem to be correlated with bursts in AE activity signaling small slip episodes that are not recorded by macroscopic strain measurements.

Changes in fractal dimension,  $D$ , suggest space–time varying clustering of AEs during loading and large slip. Such changes in  $D$  mirror the development of preferred slip orientations observed in AE focal mechanisms (Fig. 7c, d). As expected,  $D$  values for most slip events start at a value of about 2, which reflects AE activity along the localized fault zone, and then decrease towards failure on rough faults but less so for sawcuts.

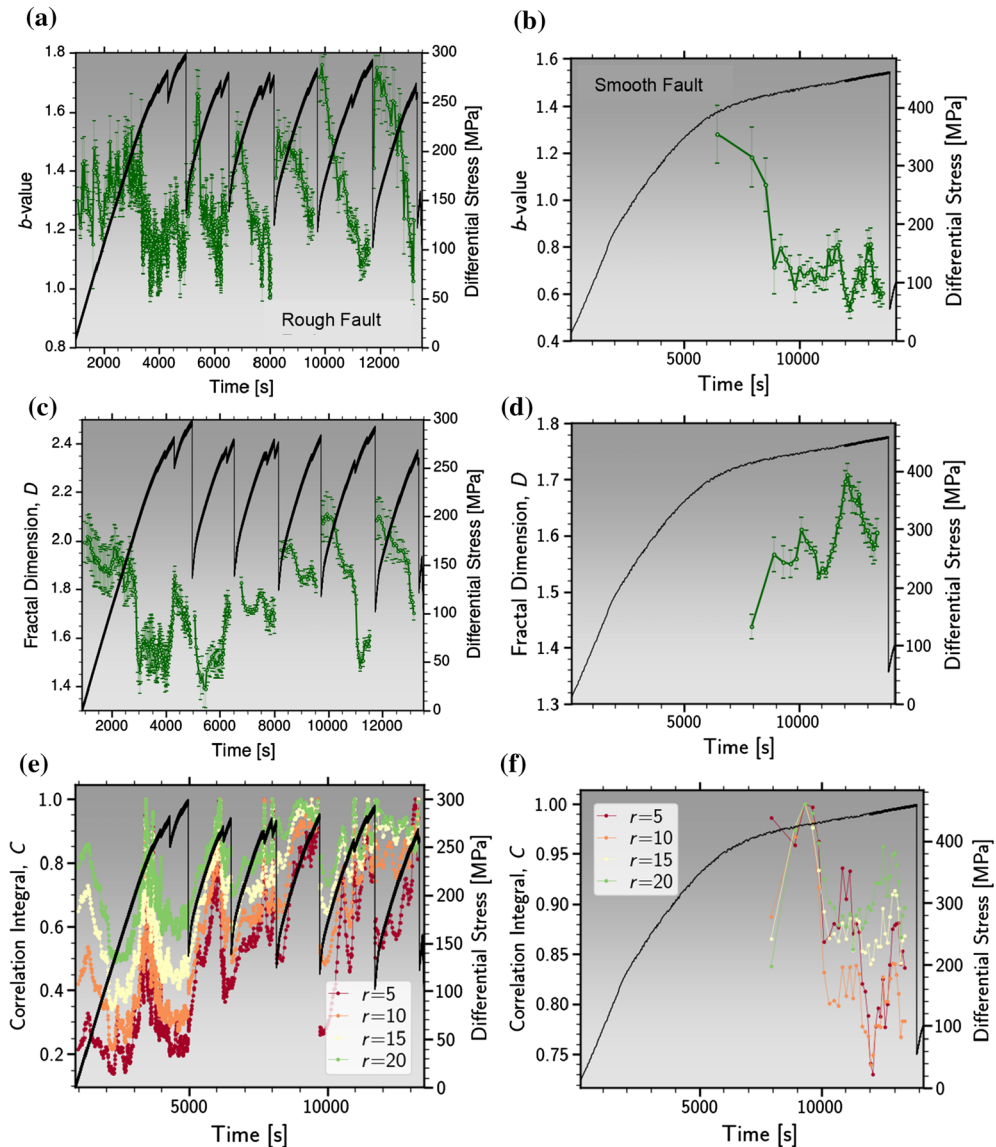


Figure 7

(a)  $b$ -value evolution versus time for rough and (b) sawcut faults. For many slip events  $b$ -values decrease prior to small or large events. (c) Correlation dimension  $D$  for rough and (d) sawcut faults.  $D$  often decreases below 2 (planar distribution of AEs) approaching a slip event suggesting activation of AE clusters along the fault. (e) correlation integral  $C$  for maximum separation distance  $r$  between 5–20 mm for rough and (f) sawcut faults. For rough faults several slip events are preceded by a peak in of the correlation function  $C(r)$  indicating strong clustering of AE events prior to failure

In addition, temporal changes of spatial correlation of AEs at fixed scales,  $C(r = 5\text{--}20\text{ mm})$  show a progressive change with loading (Fig. 7e, f). For rough faults, we find that several slip events are preceded by peaks of the correlation function suggesting progressive clustering of AEs towards the onset of sliding.

### 3.4. Strain Localization and Seismic Coupling

At the start of a stick–slip loading cycle, axial displacement of the entire sample assembly inferred from LVDT measurements corresponds closely to local measurements from strain gages placed on the sample blocks on opposing sides of the faults. This indicates that initially faults are locked. During such

periods of locking the strain gages record linear axial shortening of the entire sample assembly that is largely elastic (Figs. 2, 8). When approaching failure, the strain gage signals differ progressively from stiffness-corrected LVDT displacement data indicating a slow and gradual onset of localized sliding along the fault (Fig. 8). As faults start to slip, a progressively smaller amount of elastic sample shortening is accommodated by the opposing fault blocks. This is also expressed in the loading curves by a pronounced transition from linear to nonlinear stress increase at the yield point.

For smooth faults, sliding starts prior to failure at about 90–95% peak stress,  $\sigma_P$ , but for rough faults sliding starts at about 85–90%  $\sigma_P$  or even earlier (Fig. 8a, b). This corresponds to the different yield

stresses that are lower for samples containing rough faults compared to smooth sawcut faults. Differential stresses at the onset of sliding are typically higher for smooth faults compared to rough faults, i.e., average frictional strength and shear traction acting across rough faults is lower (Fig. 2). Also, peak stresses at failure are higher for smooth faults at our experimental conditions and stored elastic energy at the onset of sliding is significantly larger. In rough faults, shear strain is progressively localized into slip bands embedded in the damage zone in agreement with the observed shift in AE activity (Fig. 5). Irrespective of the progressively localized slip along the fault, load on the sample assembly and local shear stresses in the fault zone continue to increase toward peak strength. In contrast, smooth faults remain locked almost up to peak stress with only minor premonitory sliding before large slip events.

At peak stress  $\sigma_P$ , the seismic coupling  $\chi$  (Eq. 6) is about 0.01% for rough faults and about 0.1% for sawcut faults (cyan lines in Fig. 8). This agrees with significantly larger moment rates produced during sliding of smooth compared to rough faults (Fig. 6b).

## 4. Discussion

### 4.1. Inter-Slip Loading, Failure Preparation and Foreshocks

Earthquake preparation has been argued to be an accelerating process involving premonitory slip that may last for weeks or possibly years before the mainshock occurs. The preparatory phase may consist of any combination of aseismic transient creep events, slow slip and tremor events and progressive foreshock activity (e.g., Jones and Molnar 1979; Bouchon et al. 2013). Seismic foreshock activity preceding large earthquakes has long been suggested a precursor phenomenon potentially useful for earthquake forecasting (e.g., Jones and Molnar 1976,1979; Mignan 2014) but foreshocks prior to a larger earthquake are also frequently missing. Giulia and Wiemer (2019) recently suggested that seismic  $b$ -value variations can help to discriminate between foreshocks and mainshocks. However, as of now, foreshocks are only defined in retrospect and no

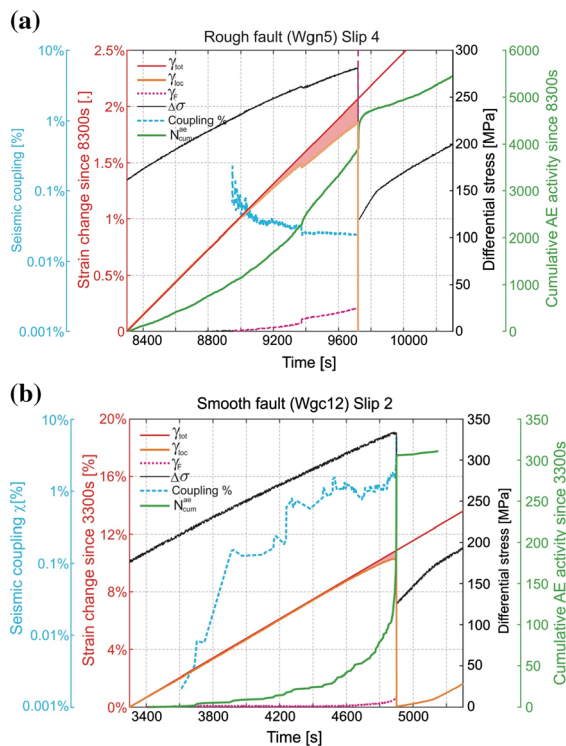


Figure 8

Difference (pink shape fill) between strain  $\gamma_{tot}$  calculated from LVDT recordings and from axial strain gages  $\gamma_{loc}$  for tested samples indicating onset of slip along faults during loading beyond yield stress. Onset of localized sliding occurs at lower stresses for rough faults (a) compared to sawcut samples (b), which remain locked almost up to peak stress. Cyan dashed lines indicate seismic coupling as defined in Eq. (7). Temporal changes in differential stress and cumulative AE activity are shown as black and green lines, respectively

unique relationship has been found between foreshock signatures and subsequent mainshock magnitude (Lipiello et al. 2012). This is illustrated by recent studies of small events detected with template matching across southern California, highlighting that > 70% of larger earthquakes are preceded by foreshocks (Trugman and Ross 2019). However, analyzing the same catalog using an alternative approach, van den Ende and Ampuero (2020) identify a significantly smaller fraction (33%) of these events displaying foreshocks.

It is well established that higher heat flow and fluid content leads to a larger fraction of foreshocks in earthquake clusters (e.g., McGuire et al. 2005; Zaliapin and Ben-Zion 2016). Analytical and numerical results in a viscoelastic damage rheology model indicate that the effective viscosity of rocks (associated with the ratio of between a brittle damage timescale and Maxwell viscous timescale) influences strongly the form of earthquake clusters and seismic coupling coefficient (Ben-Zion and Lyakhovsky 2006). In the results of this study and many other laboratory studies, foreshocks of stick–slip events are frequently reported (Lei 2003; Goebel et al. 2012; Selvadurai and Glaser 2015; Passelegue et al. 2017; Riviere et al. 2018). The detailed results presented in this work show that foreshock activity, *b*-value evolution and premonitory signatures are largely controlled by fault structure, which in turn determines stress distribution and affects rupture dynamics in the fault zone (e.g., Romanet et al. 2018).

Newly fractured specimens with rough surfaces may be regarded as laboratory equivalents of juvenile faults with a broad damage zone and small cumulative displacement, in contrast to sawcut samples that may represent mature faults with low roughness, localized strain and more homogeneous stress distribution (Goebel et al. 2017). In both cases, loading produces a nonlinear increase in cumulative AE number signaling accelerating slip; however, rough faults show more prominent seismic activity during the preparation phase of large events. Such an acceleration of AE activity has also been found before fracture nucleation in triaxial tests on intact specimens, (e.g., Lei et al. 2000; Thompson et al. 2005), samples containing joints (Journiaux et al.

2001) and stick–slip friction (Thompson et al. 2009; Goebel et al. 2012).

The stress at onset of premonitory fault slip (Fig. 4) corresponds approximately to the yield point of the loading curves (Fig. 4; McLaskey and Lockner 2014) and is often indicated by increased AE rates. In our tests, slip along the fault starts once the macroscopic yield stress is reached, and for rough faults is accompanied by progressive shear localization towards one or more slip bands constituting the fault zone (Figs. 2, 4). Evolution of rough faults involves formation of anastomosing shear bands within a broader damage zone similar to process or damage zones surrounding incipient faults propagating through intact rock (Zang et al. 2000; Lennartz-Sassinek et al. 2014). Damage zone width of rough faults significantly exceeds damage surrounding narrow sawcut faults (Fig. 4). The decay of crack, AE and fracture density with distance to the fault core observed in lab tests on intact and faulted samples (Goebel et al. 2014) was also reported in field studies of faults with a wide range of fault lengths and displacements (e.g., Scholz et al. 1993; Vermilye and Scholz 1998; Mitchell and Faulkner 2009; Savage and Brodsky 2011) and in numerical modelling of off-fault damage (Xu et al. 2012; Johri et al. 2014). In these studies, the decay in crack and fracture density has been inferred to follow a power-law, logarithmic or exponential trend.

Increasing localized shear strain in slip bands is also indicated by progressive concentration of AE hypocenters along the fault trace (Figs. 4, 5). Ben-Zion and Zaliapin (2020) recently showed several cases where prior to large earthquakes seismicity tended to localize into narrower fault zones and also coalesce into larger clusters. Regardless of fault roughness we also found increasing homogeneity of fault planes from AE focal mechanisms approaching failure (Fig. 6a). In general, rough faults display larger fault plane variability compared to smooth faults. It is conceivable that fault plane variability may serve as a proxy for fault roughness at seismogenic depth.

Cumulative event number, seismic moment rate and shear strain evolution all follow a power-law indicative of an accelerating run-away process with total slip rate evolving as:

$$\dot{D}_{(t)} = \dot{D}_{(0)} * B^n, \quad (7)$$

Where  $\dot{D}_{(t)}$ ,  $\dot{D}_{(0)}$  are slip rate and initial slip rate, respectively.  $B$  is a non-dimensional loading parameter characterizing, for example, local stress evolution and  $n$  is a constant, depending on fault topography, effective confining pressure and fault constitutive behavior. This form of avalanching damage accumulation towards failure signaled by seismic activity is commonly observed in brittle fracture experiments (Girard et al. 2010; Renard et al. 2018) and has often been reported preceding some earthquakes (Mignan 2011).

For rough and sawcut samples, we find a clear trend of decreasing  $b$ -values as stick-slip failure is approached (Fig. 7a, b). This is in agreement with numerous previous experimental studies of brittle fracture (e.g., Scholz 1968; Main et al. 1989; Lei et al. 2000; Thompson et al. 2005) and frictional sliding (Goebel et al. 2013; Riviere et al. 2018). Fluctuation of  $b$ -values have also been observed prior to large earthquakes (Smith 1981). A significant  $b$ -value decrease has been reported to precede the large 2014 Iquique and the 2011 Tohoku earthquakes (Nanjo et al. 2012, Schurr et al. 2014) and more recently the 2020,  $M_w = 6.4$  event in Puerto Rico (Dascher-Cousineau et al. 2020).

The striking observation is that  $b$ -values consistently start decreasing with progressive shear localization (Goebel et al. 2017) well before laboratory failure finally occurs suggesting growth and coalescence of microcracks that finally lead to macroscopic slip events. This process may be analogous to what has been proposed for faulting in intact brittle rocks due to clustering of interacting microcracks defining a fault nucleation patch (Reches and Lockner 1994; Reches 1999). The change of  $b$ -values approaching failure has been related inversely to global and local stress changes and progressive evolution of crack damage (Scholz 1968; Main et al. 1989; Goebel et al. 2013). This evolution starts approximately with the onset of shearing along fault and damage zone or even before, suggesting that the preparation process of an upcoming slip events is long-lasting and may even involve the final afterslip phase of the preceding slip event.

In stick-slip tests,  $b$ -values typically recover and increase significantly after failure (Goebel et al. 2013; Fig. 7a). Recently, Gulia and Wiemer (2019) suggested to estimate temporal trends in  $b$ -value before ( $b$ -value decrease) and after ( $b$ -value increase) large events to potentially identify foreshocks in real time. However, temporal changes of  $b$ -values as observed from foreshock-mainshock sequences observed in the field remain difficult to interpret (Dascher-Cousineau et al. 2020; Gulia et al. 2020).

#### 4.2. Asperity Failure and Yield Stress

Our experiments have been performed on Westerly granite samples at room temperature. Direct observation of post-mortem microstructures and AE activity indicate that deformation in the samples is accommodated entirely by brittle processes, i.e., the formation and coalescence of microcracks, grain comminution and granular flow govern inter-slip loading periods and slip events. However, only a small fraction of the total deformation is accommodated by slip generating high-frequency acoustic events with frequencies  $> 100$  KHz. Aseismic deformation is accommodated by lower frequency (slow) slip possibly assisted by brittle creep.

Our observations indicate that nucleation of unstable large slip events along rough faults is linked to a failure process of individual asperities by evolving crack damage similar to processes leading to fracture of intact specimen (Lockner et al. 1991, Reches 1999; Lei 2003; Thompson et al. 2009; Renard et al. 2018). However, for sawcut faults, dominant asperities are difficult to identify based on visual inspection alone and may rather be expressed by patches of clustered AE activity. It is conceivable that debris produced during slip events in smooth sawcut faults introduces non-stationary local gouge patches with different frictional properties that may serve as asperities. For fresh fractured faults, Goebel et al. (2012) found that roughness produces heterogeneous AE distribution across the fault. Rough faults display undulating and anastomosing slip surfaces enclosing ellipsoidal fragments that may represent larger asperities contained in the fault zone (Fig. 4).



Yabe et al. (2003) suggested a bi-modal contact model with small asperities on the grain-scale or below and larger long-wavelength asperities consisting of multiple grains. Rupture of grain-scale asperities may produce single or clustered AEs as opposed to the rupture of larger asperities along rough faults that may be linked to AE bursts and  $b$ -value drops. This is in agreement with observations of Goebel et al. (2012) as well as AE foreshock distribution and activity patches observed here preceding slip events.

#### 4.2.1 Failure of Grain-Scale Asperities

Loading of rough faults yields AE activity at differential stresses well below the macroscopic yield stress. Assuming that some AE events during loading result from formation and propagation of microcracks through grain-scale asperities exposed in the fault (Yabe et al. 2003), we may estimate the average shear stress at failure of a single asperity  $\bar{\sigma}_A^{\text{cr}}$  with radius  $r$  embedded in a low-stress environment (Sammis and Rice 2001):

$$\bar{\sigma}_A^{\text{cr}} = 1.1 K_{\text{IC}} / \sqrt{r}, \quad (8)$$

where  $K_{\text{IC}}$  is the critical stress intensity factor of Westerly granite. Assuming  $K_{\text{IC}} = 1 \text{ MPa m}^{0.5}$  (Atkinson and Meredith 1987), and  $r$  scaling with average grain size  $a = 750 \text{ }\mu\text{m}$ , we estimate the shear stresses required for onset of AE activity of about 40 MPa or less. This agrees with our observation on rough faults where minor AE activity already starts at shear stresses  $< 50 \text{ MPa}$  and differential stresses  $< 100 \text{ MPa}$  (Fig. 2).

#### 4.2.2 Yield Stress and Failure of Larger Asperities in Rough Faults

Slip along the faults starts at yield stress i.e., once stresses operating in wall rock and the fault reach a critical level. At this critical stress, slip initiates when larger asperities are fractured by microcracking and sliding occurs along preexisting defects such as grain contacts and grain boundaries. Similar to observations from intact rock failure, the formation of microcracks under elevated confining pressures is expected to involve initiation and propagation of

wing cracks (e.g., Brace and Bombolakis 1963; Ashby and Hallam 1986). Crack initiation and crack propagation have previously been correlated with the yield point of intact samples, i.e., the departure from approximate linearity of the loading curve of intact samples. Yielding and the onset of dilatant cracking are expected to occur once a critical stress level is reached (Ashby and Sammis 1990):

$$\sigma_1 = \sigma_3 \frac{(1 + \mu^2)^{0.5} + \mu}{(1 + \mu^2)^{0.5} - \mu} - \frac{\sqrt{3}}{(1 + \mu^2)^{0.5} - \mu} \frac{K_{\text{IC}}}{\sqrt{\pi c}}. \quad (9)$$

Here  $\mu$  is static friction coefficient,  $K_{\text{IC}}$  is critical stress intensity factor of Westerly granite and  $2c$  is initial crack length. Assuming  $K_{\text{IC}} = 1 \text{ MPa m}^{0.5}$  (Atkinson and Meredith 1987),  $\mu = 0.6$ ,  $c = 750 \text{ }\mu\text{m}$ , we find that yield stresses for a faulted sample to range between 200 and 250 MPa. These values represent upper bounds for the onset of failure of larger asperities in a faulted and fully locked specimen, in good agreement with our experimental observations.

#### 4.3. Strain Partitioning, Seismic Coupling and Aseismic Slip Close to Failure

Preparatory slip along rough faults initiates at lower stresses compared to peak stress on sawcuts. This may be due to average contact area  $A_r$  of rough surfaces being smaller compared to sawcut faults and average shear stress  $\bar{\sigma}$  acting on asperity contact areas therefore being higher. The average stress  $\bar{\sigma}_A$  across contact areas (asperities) of a fault may be expressed as (Jones and Molnar 1979):

$$\bar{\sigma}_A = \sigma_0 A_0 / A_r, \quad (10)$$

where  $\sigma_0$  is the remote stress acting across the fault and  $A_0$  is the fault area. Assuming that the critical stress across asperities required for onset of sliding only depends on the material and damage state, the critical stress is expected to increase as contact area  $A_r$  gets larger due to a decrease in roughness and/or increase in confining pressure (Ohnaka 2004; Selvadurai and Glaser 2015). This is in agreement with our observation of the yield stress being higher for sawcut faults.

Seismic moment release rates preceding failure and during rupture differ considerably between

smooth and rough faults (Fig. 6b). With progressive deformation and sliding along the faults, moment release rates increase less rapidly and even saturate at a constant level for rough faults. During initial loading when faults are fully or largely locked, the increase in AE moment rates is fully determined by the accumulating elastic energy due to loading of the sample. This relationship between stored elastic energy and release of seismic energy changes markedly at the onset of macroscopic sliding. The decrease in proportion of seismic energy release is possibly caused by inelastic effects and increased aseismic slip accommodated by brittle creep.

Although the number of AE events observed up to peak stress is significantly smaller for smooth faults, the total seismic moment release is larger, with smooth sawcuts hosting larger events. This is consistent with a recent study of scaling between observed maximum earthquake magnitudes, fault length, displacement and slip rates of  $> 20$  active strike-slip faults (Martínez-Garzón et al. 2015). The results from that study indicate that faults with larger displacements and smoother geometric properties also produce larger earthquakes (Martínez-Garzón et al. 2015).

Comparing total shear strain during slip prior to a large slip event with cumulative strain accrued from seismic slip along microcracks in varying orientations (Kostrov 1974) reveals that dynamic events radiating AEs represent only a very small fraction of the sample strain ( $\leq 1\%$ , Fig. 3). Also, comparing total cumulative moment of AEs ( $\approx 10^2$  Nm for saw-cut) during a stick-slip cycle to the moment of a large slip event ( $\approx 10^6$  Nm) shows that seismic events contribute only a very small fraction to the total moment of a large slip event. In other words, fault slip during rupture preparation and during slip events is largely accommodated by slip outside the frequency band of the AE transducers, i.e., below 100 kHz, contributing to brittle premonitory creep. Note, however, that coupling parameters of natural seismicity are generally higher than observed in our experiments (Scholz and Campos 2012). This may be due to the bandwidth of AE recordings limited to very high-frequencies. Interestingly, our results from stick-slip along pre-existing faults are comparable to previous studies of fracture tests performed on granite samples that have

shown only a small fraction ( $< 5\%$ ) of cracks produced AEs representing  $< 2\%$  of the total energy dissipated in the tests (Lockner et al. 1992, Zang et al. 2000).

We note that seismic coupling is not always constant during stick-slip. During loading to peak stress,  $\sigma_p$ , and with increasing amount of precursory slip, seismic coupling decreased slightly for rough faults and then remained constant. For sawcut faults coupling increased up to failure indicating that partitioning between aseismic and seismic deformation is not constant during the loading cycle.

#### 4.4. Connecting Fault Mechanics in Laboratory and Nature

The experimental observations suggest that deformation processes governing the preparatory phase of earthquakes on a pre-existing fault display signatures that may also be observed in the field. Foreshocks are typically defined in retrospect and foreshock abundance is still a matter of debate (Trugman and Ross 2019; van der Ende and Ampuero 2020). Foreshock occurrence may be related to fault structure, fault zone roughness and constitutive properties of the fault gouge, along with ambient conditions such as temperature and fluid content, which also govern the partitioning between seismic and aseismic deformation events (e.g., Ben-Zion 2008). This is shown by our experimental results that are in agreement with predictions from modeling (e.g., Kazemian et al. 2015) and with damage rheology model results of Ben-Zion and Lyakhovsky (2006) using the concept of effective viscosity. In addition to fault structure and stress heterogeneity, foreshock activity may also depend on strain rate (Ojala et al. 2004). Our experiments show that strong structural and stress heterogeneity is expected to result in reduced seismic coupling and potentially more prominent foreshock activity, compared to deformation along more homogeneous and geometrically simpler fault segments. The experimental results indicate that preparatory processes appear to be long-lasting and continuous in agreement with recent observations from large earthquakes (e.g., Mavrommatis et al. 2014; Socquet et al. 2017). This suggests that a separation between preslip and cascade conceptual models may not be

warranted as both, aseismic and seismic processes are involved in shear deformation leading to failure. However, their respective contributions may vary significantly depending of fault structure and constitutive properties of the fault zone material.

We note that generation of large earthquakes involves generally also localization of deformation onto the main rupture zones (e.g., Lyakhovsky et al. 2001; McBeck et al. 2020; Ben-Zion and Zaliapin 2020). Progressive healing of faulted materials during long inter-seismic periods (e.g., Reches 1999; Muhuri et al. 2003; Aben et al. 2017; Pei et al. 2019) requires some form of re-localization onto pre-existing faults before subsequent large earthquakes (e.g., Ben-Zion and Zaliapin 2020). Detailed analysis of localization processes in our AE data is deferred to a future work.

### 5. Conclusions

We analyzed the rupture preparation process of stick slip events in a series of triaxial tests performed on Westerly granite samples with rough and smooth fault surfaces. Rupture preparation is a long-lasting process involving progressive decoupling and slip accommodated by seismic and aseismic shear. Preparatory fault slip is accelerating over the entire inter-slip loading periods and is accompanied by seismic (AE) activity. Increasing rates of AE are punctuated by distinct peaks associated with relatively large slip events. Damage evolution along the faults and surrounding wall rocks is tracked by precursory decrease of seismic *b*-values and correlation dimension, and peaks in spatial event correlation, suggesting that nucleation of large slip events and propagation occurs by failure of multiple asperities. Shear strain estimated from AEs represents only a small fraction (< 1%) of total shear strain accumulated during the slip preparation phase and during a system-size slip event. Seismic coupling is larger for sawcut faults compared to rough faults and decreases for both fault types towards failure, with rough faults showing a more pronounced contribution of aseismic deformation leading up to failure.

### Acknowledgments

We thank reviewers Ian Main and Art McGarr for their constructive comments that helped to improve the manuscript, Stefan Gehrmann for sample preparation and Michael Naumann for technical support at GFZ-Potsdam. GK acknowledges support from the Deutsche Forschungsgemeinschaft (DFG), Grant KW 84/4-1 T. Goebel and Y. Ben-Zion were supported by GFZ and the German Alexander von Humboldt Foundation during several visits to GFZ

**Author contributions** All authors contributed to the study. Material preparation, data collection and analysis were performed by all authors. The first draft of the manuscript was written by GD and all authors commented on previous versions of the manuscript. All authors read and approved the final manuscript.

### Funding

Open Access funding enabled and organized by Projekt DEAL. GD acknowledges support from GFZ.

### Compliance with ethical standards

**Conflict of interest** Not relevant.

**Availability of data and material** All experimental data is available from the authors.

**Code availability** Not relevant.

**Open Access** This article is licensed under a Creative Commons Attribution 4.0 International License, which permits use, sharing, adaptation, distribution and reproduction in any medium or format, as long as you give appropriate credit to the original author(s) and the source, provide a link to the Creative Commons licence, and indicate if changes were made. The images or other third party material in this article are included in the article's Creative Commons licence, unless indicated otherwise in a credit line to the material. If material is not included in the article's Creative Commons licence and your intended use is not permitted by statutory regulation or exceeds the permitted use, you will need to obtain permission directly from the copyright holder. To view a copy of this licence, visit <http://creativecommons.org/licenses/by/4.0/>.

**Publisher's Note** Springer Nature remains neutral with regard to jurisdictional claims in published maps and institutional affiliations.

## REFERENCES

- Aben, F. M., Doan, M. L., Gratier, J. P., & Renard, F. (2017). Experimental postseismic recovery of fractured rocks assisted by calcite sealing. *Geophysical Research Letters*, *44*, 7228–7238.
- Abercrombie, R. E., Bannister, S., Ristau, J., & Doser, D. (2017). Variability of earthquake stress drop in a subduction setting, the Hikurangi Margin, New Zealand. *Geophysical Journal International*, *208*, 306–320. <https://doi.org/10.1093/gji/ggw393>
- Aki, K. (1965). Maximum likelihood estimate of  $b$  in the formula  $\log N = a - bM$  and its confidence limits. *Bulletin of the Earthquake Research Institute of Tokyo University*, *43*, 237–239.
- Ampuero, J.-P., Rippberger, J., & Mai, P. M. (2006). Properties of dynamic earthquake ruptures with heterogeneous stress drop. In R. Abercrombie, A. McGarr, G. Di Toro, G. & H. Kanamori (Eds.), *Earthquakes: Radiated energy and the physics of faulting*. <https://doi.org/10.1029/170GM25>
- Ashby, M. F., & Hallam, S. D. (1986). The failure of brittle solids containing small cracks under compressive stress states. *Acta Metallurgica*, *34*, 497–510.
- Ashby, M. F., & Sammis, C. G. (1990). The damage mechanics of brittle solids in compression. *Pure and Applied Geophysics*, *33*, 489–521.
- Avouac, J.-P. (2015). From geodetic imaging of seismic and aseismic fault slip to dynamic modeling of the seismic cycle. *Annual Review of Earth and Planetary Sciences*, *43*, 233–271.
- Bakun, W. H., et al. (2005). Implications for prediction and hazard assessment from the 2004 Parkfield earthquake. *Nature*, *437*, 969–974. <https://doi.org/10.1038/nature04067>
- Ben Zion, Y., & Sammis, C. (2003). Characterization of fault zones. *Pure Applied Geophysical*, *160*, 677–715. <https://doi.org/10.1007/PL00012554>
- Ben-David, O., & Fineberg, J. (2011). Static friction coefficient is not a material constant. *Physical Review Letters*, *106*, 254301. <https://doi.org/10.1103/PhysRevLett.106.254301>
- Ben-Zion, Y. (2008). Collective behavior of earthquakes and faults: Continuum-discrete transitions, evolutionary changes and corresponding dynamic regimes. *Reviews of Geophysics*, *46*. <https://doi.org/10.1029/2008RG000260>
- Ben-Zion, Y., & Lyakhovskiy, V. (2006). Analysis of aftershocks in a lithospheric model with seismogenic zone governed by damage rheology. *Geophysical Journal International*, *165*, 197–210. <https://doi.org/10.1111/j.1365-246X.2006.02878.x>
- Ben-Zion, Y., & Rice, J. R. (1993). Earthquake failure sequences along a cellular fault zone in a three-dimensional elastic solid containing asperity and nonasperity regions. *Journal of Geophysical Research*, *98*, 14109–14131.
- Ben-Zion, Y., Rockwell, T., Shi, Z., & Xu, S. (2012). Reversed-polarity secondary deformation structures near fault stepovers. *Journal of Applied Mechanics*, *79*, 031025. <https://doi.org/10.1115/1.4006154>
- Ben-Zion, Y., Eneva, M., & Liu, Y. (2003). Large earthquake cycles and intermittent criticality on heterogeneous faults due to evolving stress and seismicity. *Journal of Geophysical Research*. <https://doi.org/10.1029/2002JB002121>.
- Ben-Zion, Y., & Zaliapin, I. (2020). Localization and coalescence of seismicity before large earthquakes. *Geophysical Journal International*, *223*, 561–583. <https://doi.org/10.1093/gji/ggaa315>
- Bouchon, M., Durand, V., Marsan, D., Karabulut, H., & Schmittbuhl, J. (2013). The long precursory phase of most large interplate earthquakes. *Nature Geoscience*, *6*, 299–302. <https://doi.org/10.1038/NGEO1770>
- Brace, W. F., & Bombolakis, E. G. (1963). A note on brittle crack growth in compression. *Journal of Geophysical Research*, *68*, 3709–3713.
- Brace, W. F., & Byerlee, J. D. (1966). Stick-slip as a mechanism for earthquakes. *Science*, *153*, 990–992.
- Brodsky, E. E., & Lay, T. (2014). Recognizing foreshocks from the 1 April 2014 Chile Earthquake. *Science*, *344*, 700–702.
- Candela, T., Renard, F., Bouchon, M., Schmittbuhl, J., & Brodsky, E. E. (2011). Stress drop during earthquakes: Effect of fault roughness scaling. *Bulletin of the Seismological Society of America*, *101*, 2369–2387. <https://doi.org/10.1785/0120100298>
- Clauset, A., Shalizi, C. R., & Newmann, M. E. J. (2009). Power-law distributions in empirical data. *SIAM Review*, *51*(4), 661–703.
- Cocco, M., Tinti, E., & Cirella, A. (2016). On the scale dependence of earthquake stress drop. *Journal of Seismology*, *20*, 1151–1170. <https://doi.org/10.1007/s10950-016-9594-4>
- Cochard, A., & Madariaga, R. (1994). Dynamic faulting under rate-dependent friction. *Pure Applied Geophysical*, *142*, 419–445. <https://doi.org/10.1007/BF00876049>
- Dascher-Cousineau, K., Lay, T., & Brodsky, E. E. (2020). Two foreshock sequences post Gulia and Wiemer (2019). *Seismological Research Letters*, *91*, 2843–2850. <https://doi.org/10.1785/0220200082>
- Delouis, B., Giardini, D., Lundgren, P., & Salichon, J. (2002). Joint inversion of InSAR, GPS, teleseismic, and strong-motion data for the spatial and temporal distribution of earthquake slip: Application to the 1999 Izmit Mainshock. *Bulletin of the Seismological Society of America*, *92*(1), 278–299.
- Dieterich, J. H. (1978). Preseismic fault slip and earthquake prediction. *Journal of Geophysical Research*, *83*, 3940–3948.
- Dieterich, J. H. (1979). Modeling of rock friction, 2. Simulation of preseismic slip. *Journal of Geophysical Research*, *84*, 2169–2175.
- Dieterich, J. H. (1992). Earthquake nucleation on faults with rate- and state-dependent strength. *Tectonophysics*, *211*, 115–134. [https://doi.org/10.1016/0040-1951\(92\)90055-B](https://doi.org/10.1016/0040-1951(92)90055-B)
- Durand, V., Bentz, S., Kwiatek, G., Dresen, G., Wollin, C., Heidebach, O., et al. (2020). A two-scale preparation phase preceded an  $M_w$  5.8 earthquake in the Sea of Marmara Offshore Istanbul, Turkey. *Seismological Research Letters*. <https://doi.org/10.1785/0220200110>.
- Ellsworth, W. L., & Beroza, G. C. (1995). Seismic evidence for an earthquake nucleation phase. *Science*, *268*, 851–855.
- Ellsworth, W. L., & Bulut, F. (2018). Nucleation of the 1999 Izmit earthquake by a triggered cascade of foreshocks. *Nature Geoscience*. <https://doi.org/10.1038/s41561-018-0145-1>
- Fletcher, J. B., & McGarr, A. (2006). Distribution of stress drop, stiffness, and fracture energy over earthquake rupture zones. *Journal of Geophysical Research*, *111*. <https://doi.org/10.1029/2004JB003396>
- Frank, W., Rousset, B., Lasserre, C., & Campillo, M. (2018). Revealing the cluster of slow transients behind a large slow slip event. *Science Advances*, *4*. <https://doi.org/10.1126/sciadv.aat0661>
- Girard, L., Amitrano, D., & Weiss, J. (2010). Failure as a critical phenomenon in a progressive damage model. *Journal of*



- Statistical Mechanics*. <https://doi.org/10.1088/1742-5468/2010/01/P01013>
- Goebel, T.H.W., Becker, T.W., Schorlemmer, D., Stanchits, S., Sammis, C., Rybacki, E., and Dresen, G. (2012). Identifying fault heterogeneity through mapping spatial anomalies in acoustic emission statistics. *Journal of Geophysical Research*, 117. <https://doi.org/10.1029/2011JB008763>
- Goebel, T. H. W., Candela, T., Sammis, C. G., Becker, T. W., Dresen, G., & Schorlemmer, D. (2014). Seismic event distributions and off-fault damage during frictional sliding of saw-cut surfaces with pre-defined roughness. *Geophysical Journal International*, 196(1), 612–625. <https://doi.org/10.1093/gji/ggt401>
- Goebel, T. H. W., Kwiatek, G., Becker, T. W., Brodsky, E. E., & Dresen, G. (2017). What allows seismic events to grow big?: Insights from b-value and fault roughness analysis in laboratory stick–slip experiments. *Geology*, 45(9), 815–818. <https://doi.org/10.1130/G39147.1>
- Goebel, T. H. W., Schorlemmer, D., Becker, T. W., Dresen, G., & Sammis, C. G. (2013). Acoustic emissions document stress changes over many seismic cycles in stick–slip experiments. *Geophysical Research Letters*, 40, 2049–2054. <https://doi.org/10.1002/grl.12057>
- Grassberger, P. (1983). Generalized dimensions of strange attractors. *Physics Letters A*, 97(6), 227–230.
- Gulia, L., & Wiemer, S. (2019). Real-time discrimination of earthquake foreshocks and aftershocks. *Nature*, 574, 193–199. <https://doi.org/10.1038/s41586-019-1606-4>
- Gulia, L., Wiemer, S., & Vannucci, G. (2020). *Prospective evaluation of the foreshock traffic light system in Ridgecrest and implications for aftershock hazard assessment*. Seismol: Research Letters. <https://doi.org/10.1785/0220190307>
- Guo, Z., & Ogata, Y. (1997). Statistical relations between the parameters of aftershocks in time, space, and magnitude. *Journal of Geophysical Research*, 102(B2), 2857–2873.
- Hanks, T. C., & Kanamori, H. (1979). A moment magnitude scale. *Journal of Geophysical Research*, 84, 2348–2350.
- Hasegawa, A. & Yoshida, K. (2015). Preceding seismic activity and slow slip events in the source area of the 2011 Mw 9.0 Tohoku-Oki earthquake: a review. *Geoscience Letters*. 2. <https://doi.org/10.1186/s40562-015-0025-0>
- Henderson, J., & Main, I. (1992). A simple fracture-mechanical model for the evolution of seismicity. *Geophysical Research Letters*, 19(4), 365–368.
- Ida, Y. (1972). Cohesive force across the tip of a longitudinal-shear crack and Griffith's specific surface energy. *Journal of Geophysical Research*, 77, 3796–3805.
- Johri, M., Dunham, E. M., Zoback, M. D., & Fang, Z. (2014). Predicting fault damage zones by modeling dynamic rupture propagation and comparison with field observations. *Journal of Geophysical Research Solid Earth*, 119. <https://doi.org/10.1002/2013JB010335>
- Jones, L., & Molnar, P. (1976). Frequency of foreshocks. *Nature*, 262, 677–679.
- Jones, L., & Molnar, P. (1979). Some characteristics of foreshocks and their possible relationship to earthquake prediction and premonitory slip on faults. *Journal of Geophysical Research*, 84, 3596–3608.
- Journiaux, L., Masuda, K., Lei, X., Kusunose, K., Liu, L., & Ma, W. (2001). Comparison of the microfracture localization in granite between fracturation and slip of a preexisting macroscopic healed joint by acoustic emission measurements. *Journal of Geophysical Research*, 106, 8687–8698.
- Kagan, Y. Y. (2007). Earthquake spatial distribution: The correlation dimension. *Geophysical Journal International*, 168(3), 1175–1194. <https://doi.org/10.1111/j.1365-246X.2006.03251.x>
- Kagan, Y. Y., & Knopoff, L. (1980). Spatial distribution of earthquakes: The two-point correlation function. *Geophysical Journal International*, 62(2), 303–320. <https://doi.org/10.1111/j.1365-246X.1980.tb04857.x>
- Kammer, D. S., Radiguet, M., Ampuero, J. P., & Molinari, J. F. (2015). Linear elastic fracture mechanics predicts the propagation distance of frictional slip. *Tribology Letters*, 57, 23. <https://doi.org/10.1007/s11249-014-0451-8>
- Kazemian, J., Tiampo, K. F., Klein, W., & Dominguez, R. (2015). Foreshock and aftershocks in simple earthquake models. *Physical Review Letters*, 114, 088501. <https://doi.org/10.1103/PhysRevLett.114.088501>
- Kostrov, V. (1974). Seismic moment and energy of earthquakes and seismic flow of rock. *Earth Physics*, 1, 23–40.
- Kwiatek, G., Charalampidou, E. M., & Dresen, G. (2014a). An improved method for seismic moment tensor inversion of acoustic emissions through assessment of sensor coupling and sensitivity to incidence angle. *International Journal of Rock Mechanics and Mining Sciences*, 65, 153–161. <https://doi.org/10.1016/j.ijrmmms.2013.11.005>
- Kwiatek, G., Goebel, T. H. W., & Dresen, G. (2014b). Seismic moment tensor and b value variations over successive seismic cycles in laboratory stick–slip experiments. *Geophysical Research Letters*, 41, 5838–5846. <https://doi.org/10.1002/2014GL060159>
- Kwiatek, G., Martínez-Garzón, P., & Bohnhoff, M. (2016). HybridMT: A MATLAB/Shell environment package for seismic moment tensor inversion and refinement. *Seismological Research Letters*, 87, 964–976. <https://doi.org/10.1785/0220150251>
- Lei, X. (2003). How do asperities fracture? An experimental study of unbroken asperities. *Earth and Planetary Science Letters*, 213, 347–359.
- Lei, X., Kusunose, K., Nishizawa, O., Cho, A., & Satoh, T. (2000). On the spatio-temporal distribution of acoustic emissions in two granitic rocks under triaxial compression: the role of pre-existing cracks. *Geophysical Research Letters*, 27, 1997–2000.
- Lennartz-Sassinek, S., Main, I. G., Zaiser, M., & Graham, C. C. (2014). Acceleration and localization of subcritical crack growth in a natural composite material. *Physical Review E*, 90, 052401. <https://doi.org/10.1103/PhysRevE.90.052401>
- Lippiello, E., Marzocchi, W., de Arcangelis, L., & Godano, C. (2012). Spatial organization of foreshocks as a tool to forecast large earthquakes. *Scientific Reports*. <https://doi.org/10.1038/srep00846>
- Lyakhovskiy, V., Ben-Zion, Y., & Agnon, A. (2001). Earthquake cycle, fault zones, and seismicity patterns in a rheologically layered lithosphere. *Journal of Geophysical Research*, 106, 4103–4120.
- Mai, P. M., & Beroza, G. C. (2002). A spatial random field model to characterize complexity in earthquake fields. *Journal of Geophysical Research*, 107, 2308. <https://doi.org/10.1029/2001JB000588>
- Main, I. G. (1992). Damage mechanics with long-range interactions: Correlation between the seismic b-value and the fractal two-point correlation dimension. *Geophysical Journal International*



- International*, 111(3), 531–541. <https://doi.org/10.1111/j.1365-246X.1992.tb02110.x>
- Main, I. G., Meredith, P. G., & Jones, C. (1989). A reinterpretation of the precursory seismic b-value anomaly using fracture mechanics. *Geophysical Journal*, 96, 131–138.
- Main, I. G., Meredith, P. G., & Sammonds, P. R. (1992). Temporal variations in seismic event rate and b-values from stress corrosion constitutive laws. *Tectonophysics*, 211, 233–246.
- Martínez-Garzón, P., Ben-Zion, Y., Zaliapin I., & Bohnhoff, M. (2019). Seismic clustering in the Sea of Marmara: Implications for monitoring earthquake processes. *Tectonophysics*, 768. <https://doi.org/10.1016/j.tecto.2019.228176>
- Martínez-Garzón, P., Bohnhoff, M., Ben-Zion, Y., & Dresen, G. (2015). Scaling of maximum observed magnitudes with geometrical and stress properties of strike-slip faults. *Geophysical Research Letters*, 42, 10230–10238. <https://doi.org/10.1002/2015GL066478>
- Mavrommatis, A. P., Segall, P., & Johnson, K. M. (2014). A decadal-scale deformation transient prior to the 2011 Mw 9.0 Tohoku-oki earthquake. *Geophysical Research Letters*, 41, 4486–4494. <https://doi.org/10.1002/2014GL060139>
- McBeck, J., Ben-Zion, Y., & Renard, F. (2020). The mixology of precursory strain partitioning approaching brittle failure in rocks. *Geophysical Journal International*, 221, 1856–1872. <https://doi.org/10.1093/gji/ggaa121>
- McGuire, J. J., Boettcher, M. S., & Jordan, T. H. (2005). Foreshock sequences and short-term earthquake predictability on East Pacific Rise transform faults. *Nature*, 434(7032), 457–461.
- McLaskey, G. C., & Glaser, S. D. (2012). Acoustic emission sensor calibration for absolute source measurements. *Journal of Non-destructive Evaluation*, 31, 157–168. <https://doi.org/10.1007/s10921-012-0131-2>
- McLaskey, G. C., & Kilgore, B. D. (2013). Foreshocks during the nucleation of stick-slip instability. *Journal of Geophysical Research*, 118, 2982–2997. <https://doi.org/10.1002/jgrb.50232>
- McLaskey, G. C., & Lockner, D. A. (2014). Preslip and cascade processes initiating laboratory stick slip. *Journal of Geophysical Research*, 119, 6323–6336. <https://doi.org/10.1002/2014JB011220>
- Mignan, A. (2011). Retrospective on the accelerating seismic release (ASR) hypothesis: Controversy and new horizons. *Tectonophysics*, 505, 1–16.
- Mignan, A. (2014). The debate on the prognostic value of earthquake foreshocks: A meta-analysis. *Scientific Reports*, 4, 4099. <https://doi.org/10.1038/srep04099>
- Mitchell, T. M., & Faulkner, D. R. (2009). The nature and origin of off-fault damage surrounding strike-slip fault zones with a wide range of displacements: A field study from the Atacama fault system, northern Chile. *Journal of Structural Geology*, 31, 802–816. <https://doi.org/10.1016/j.jsg.2009.05.002>
- Moreno, M., Rosenau, M., & Oncken, O. (2010). Maule earthquake slip correlates with pre-seismic locking of Andean subduction zone. *Nature*, 467. <https://doi.org/10.1038/nature09349>
- Muhuri, S. K., Dewers, T. A., Scott-Thurman, E., & Reches, Z. (2003). Interseismic fault strengthening and earthquake-slip instability: Friction or cohesion? *Geology*, 31, 881–884.
- Nanjo, K. Z., Hirata, N., Obara, K., & Kasahara, K. (2012). Decade-scale decrease in b value prior to the M9-class 2011 Tohoku and 2004 Sumatra quakes. *Geophysical Research Letters*, 39. <https://doi.org/10.1029/2012GL052997>
- Ohnaka, M. (1992). Earthquake source nucleation: A physical model for short-term precursors. *Tectonophysics*, 211, 149–178.
- Ohnaka, M. (2004). A constitutive scaling law for shear rupture that is inherently scale-dependent, and physical scaling of nucleation time to critical point. *Pure Applied Geophysics*, 161, 1915–1929.
- Ohnaka, M., & Shen, L. (1999). Scaling of the shear rupture process from nucleation to dynamic propagation: Implications of geometric irregularity of the rupturing surfaces. *Journal of Geophysical Research*, 104, 817–844.
- Ojala, I. O., Main, I. G., & Ngwenya, B.T. (2004). Strain rate and temperature dependence of Omori law scaling constants of AE data: Implications for earthquake foreshock-aftershock sequences. *Geophysical Research Letters*, 31. <https://doi.org/10.1029/2004GL020781>
- Pacheco, J. F., Sykes, L., & Scholz, C. H. (1993). Nature of seismic coupling along simple plate boundaries of the subduction type. *Journal of Geophysical Research*, 98, 14133–14155.
- Palmer, A. C., & Rice, J. R. (1973). The growth of slip surfaces in the progressive failure of overconsolidated clay. *Proceedings of the Royal Society London A*, 332, 527–548.
- Passelegue, F., Latour, S., Schubnel, A., Nielsen, S., Bhat, H., & Madariaga, R. (2017). Influence of fault strength on precursory processes during laboratory earthquakes. In M. Thomas, T. M. Mitchell, & H. S. Bhat (Eds.), *Fault zone dynamic processes: Evolution of fault properties during seismic rupture* (Vol. 227, pp. 229–242). New York: Wiley.
- Pei, S., et al. (2019). Seismic velocity reduction and accelerated recovery due to earthquakes on the Longmenshan fault. *Nature Geoscience*, 12, 387–392.
- Popov, V. L., Grzempa, B., Starcevic, J., & Fabry, F. (2010). Accelerated creep as a precursor of frictional instability and earthquake prediction. *Physical Mesomechanics*, 13, 283–291.
- Reasenber, P. A. (1999). Foreshock occurrence before large earthquakes. *Journal of Geophysical Research*, 104, 4755–4768.
- Reches, Z. (1999). Mechanisms of slip nucleation during earthquakes. *Earth and Planetary Science Letters*, 170, 475–486.
- Reches, Z., & Lockner, D. A. (1994). Nucleation and growth of faults in brittle rocks. *Journal of Geophysical Research*, 99, 18159–18173.
- Renard, F., Weiss, J., Mathiesen, J., Ben Zion, Y., Kandula, N., & Cordonnier, B. (2018). Critical evolution of damage towards system-size failure in crystalline rock. *Journal of Geophysical Research*, 123, 1969–1986. <https://doi.org/10.1002/2017JB014964>
- Ripperger, J., Ampuero, J.-P., Mai, P. M., & Giardini, D. (2007). Earthquake source characteristics from dynamic rupture with constrained stochastic fault stress. *Journal of Geophysical Research*, 112. <https://doi.org/10.1029/2006JB004515>
- Roeloffs, E. A. (2006). Evidence for aseismic deformation rate changes prior to earthquakes. *Annual Review of Earth and Planetary Sciences*, 2006(34), 591–627. <https://doi.org/10.1146/annurev.earth.34.031405.124947>
- Romanet, P., Bhat, H. S., Jolivet, R., & Madariaga, R. (2018). Fast and slow slip events emerge due to fault geo-metrical complexity. *Geophysical Research Letters*, 45, 4809–4819. <https://doi.org/10.1029/2018GL077579>
- Sammis, C. G., & Rice, J. R. (2001). Repeating earthquakes as low-stress-drop events at a border between locked and creeping fault patches. *Bulletin of the Seismological Society America*, 91, 532–537.

- Savage, H. M., & Brodsky, E. E. (2011). Collateral damage: Evolution with displacement of fracture distribution and secondary fault strands in fault damage zones. *Journal of Geophysical Research*, *116*, B03405. <https://doi.org/10.1029/2010JB007665>
- Schmittbuhl, J., Chambon, G., Hansen, A., & Bouchon, M. (2006). Are stress distributions along faults the signature of asperity squeeze? *Geophysical Research Letters*, *33*, L13307. <https://doi.org/10.1029/2006GL025952>
- Scholz, C. H. (1968). Experimental study of the fracturing process in brittle rock. *Journal of Geophysical Research*, *73*, 1447–1454.
- Scholz, C. H. (2019). *The mechanics of earthquakes and faulting*. Cambridge: Cambridge Univ Press. <https://doi.org/10.1017/9781316681473>
- Scholz, C. H., & Campos, J. (2012). The seismic coupling of subduction zones revisited. *Journal of Geophysical Research*, *117*, B05310. <https://doi.org/10.1029/2011JB009003>
- Scholz, C. H., Dawers, N. H., Yu, J. Z., & Anders, M. H. (1993). Fault growth and fault scaling laws: Preliminary results. *Journal of Geophysical Research*, *98*, 21951–21961.
- Scholz, C. H., Molnar, P., & Johnson, T. (1972). Detailed studies of frictional studies of granite and implications for the earthquake mechanism. *Journal of Geophysical Research*, *77*, 6392–6406.
- Schurr, et al. (2014). Gradual unlocking of plate boundary-controlled initiation of the 2014 Iquique earthquake. *Nature*, *512*, 299–302. <https://doi.org/10.1038/nature13681>
- Selvadurai, P. A., & Glaser, S. D. (2015). Laboratory-developed contact models controlling instability on frictional faults. *Journal of Geophysical Research*, *120*, 4208–4236. <https://doi.org/10.1002/2014JB011690>
- Selvadurai, P. A., & Glaser, S. D. (2017). Asperity generation and its relationship to seismicity on a planar fault: A laboratory simulation. *Geophysical Journal International*, *208*, 1009–1025. <https://doi.org/10.1093/gji/ggw439>
- Smith, W. D. (1981). The b-value as an earthquake precursor. *Nature*, *289*, 136–139.
- Socquet, A., Valdes, J. P., Jara, J., Cotton, F., Walpersdorf, A., Cotte, N., Specht, S., Ortega-Culaciati, F., Carrizo, D., & Norabuena, E. (2017). An 8month slow slip event triggers progressive nucleation of the 2014 Chile megathrust. *Geophysical Research Letters*, *44*. <https://doi.org/10.1002/2017GL073023>
- Stanchits S., & Dresen, G. (2003). Separation of tensile and shear cracks based on acoustic emission analysis of rock fracture, In *Proceedings of the International Symposium: Non-Destructive Testing in Civil Engineering (NDT-CE)*, (p. 107) Berlin, Germany
- Stanchits, S., Vinciguerra, S., & Dresen, G. (2006). Ultrasonic velocities, acoustic emission characteristics and crack damage of basalt and granite. *Pure and Applied Geophysics*, *163*, 975–994. <https://doi.org/10.1007/s00024-006-0059-5>
- Thompson, B. D., Young, R. P., & Lockner, D. A. (2005). Observations of premonitory acoustic emission and slip nucleation during a stick slip experiment in smooth faulted Westerly granite. *Geophysical Research Letters*, *32*, L10304. <https://doi.org/10.1029/2005GL022750>
- Thompson, B. D., Young, R. P., & Lockner, D. A. (2009). Premonitory acoustic emissions and stick-slip in natural and smooth-faulted Westerly granite. *Journal of Geophysical Research*, *114*, B02205. <https://doi.org/10.1029/2008JB005753>
- Trugman, D. T., & Ross, Z. E. (2019). Pervasive foreshock activity across southern California. *Geophysical Research Letters*, *46*, 8772–8781. <https://doi.org/10.1029/2019GL083725>
- Utsu, T., Ogata, Y., & Ritsuko, M. (1965). The centenary of Omori formula for a decay law of afterhock activity. *Journal of Physics of the Earth*, *43*, 1–33.
- van den Ende, M. P. A., & Ampuero, J.-P. (2020). On the statistical significance of foreshock sequences in Southern California. *Geophysical Research Letters*, *47*. <https://doi.org/10.1029/2019GL086224>
- Vermilye, J. M., & Scholz, C. H. (1998). The process zone: A microstructural view of fault growth. *Journal of Geophysical Research Solid Earth*, *103*, 12223–12237.
- Wu, C., Peng, Z., Meng, X., & Ben-Zion, Y. (2014). Lack of spatio-temporal localization of foreshocks before the 1999 Mw7.1 Duzce, Turkey earthquake. *Bulletin of the Seismological Society of America*, *104*, 560–566. <https://doi.org/10.1785/0120130140>
- Wyss, M., Sammis, C. G., Nadeau, R. M., & Wiemer, S. (2004). Fractal dimension and b-value on creeping and locked patches of the San Andreas fault near Parkfield, California. *Bulletin of the Seismological Society of America*, *94*(2), 410–421. <https://doi.org/10.1785/0120030054>
- Xu, S., Ben-Zion, Y., & Ampuero, J.-P. (2012). Properties of inelastic yielding zones generated by in-plane dynamic ruptures: II. Detailed parameter-space study. *Geophysical Journal International*, *191*, 1343–1360. <https://doi.org/10.1111/j.1365-246X.2012.05685.x>
- Yabe, Y., Kato, N., Yamamoto, K., & Hirasawa, T. (2003). Effect of sliding rate on the activity of acoustic emission during stable sliding. *Pure and Applied Geophysics*, *160*, 1163–1189.
- Yoshimitsu, N., Kawakata, H., & Takahashi, N. (2014). Magnitude –7 level earthquakes: A new lower limit of self-similarity in seismic scaling relationships. *Geophysical Research Letters*, *41*, 4495–4502. <https://doi.org/10.1002/2014GL060306>
- Zaliapin, I., & Ben-Zion, Y. (2013). Earthquake clusters in southern California II: Classification and relation to physical properties of the crust. *Journal of Geophysical Research*, *118*, 2865–2877. <https://doi.org/10.1002/jgrb.50178>
- Zaliapin, I., & Ben-Zion, Y. (2016). A global classification and characterization of earthquake clusters. *Geophysical Journal International*, *207*, 608–634. <https://doi.org/10.1093/gji/ggw300>
- Zang, A., Wagner, F. C., Stanchits, S., Dresen, G., Andresen, R., & Haidekker, M. A. (1998). Source analysis of acoustic emissions in granite cores under symmetric and asymmetric compressive load. *Geophysical Journal International*, *135*, 1113–1130.
- Zang, A., Wagner, C., Stanchits, S., Janssen, C., & Dresen, G. (2000). Fracture process zone in granite. *Journal of Geophysical Research*, *105*, 23651–23661.